Mineralogical and geochemical characteristics and the genesis of the Paleoproterozoic Staicele and Gārsene Iron Ore Deposits of Latvia

VERTAISARVIOITU
KOLLEGIALT GRANSKAD
PEER-REVIEWED
www.tsv.fi/tunnus

Dmitrijs Vorobjovs[1*], Ģirts Stinkulis[1], Māris Bērtiņš[2], Artūrs Vīksna[2], Raimonds Meija[3,4] and Agnese Brangule[5]

[1] *Faculty of Science and Technology, University of Latvia, Jelgava Street 1, Riga, Latvia*
[2] *Faculty of Medicine and Life Sciences, University of Latvia, Jelgava Street 1, Riga, Latvia*
[3] *Institute of Chemical Physics, Faculty of Science and Technology, University of Latvia, Raina Boulevard 19, Riga, Latvia*
[4] *Department of Physics, Faculty of Medicine, Riga Stradins University, Dzirciema street 16, Riga, Latvia*
[5] *Department of Pharmaceutical Chemistry, Riga Stradins University, Konsula Street 21, Riga, Latvia*

Abstract

The Palaeoproterozoic crystalline basement of Latvia contains several poorly studied iron-rich formations that were last investigated in detail more than 40 years ago. This study reassesses the mineralogical and geochemical characteristics and genesis of the two best-known and most prospective occurrences, Staicele and Gārsene, using polished sections, thin sections, SEM–EDX, XRF, XRD, and ICP–MS data from archived drill core. The Staicele ores are interpreted as a metamorphosed, Mn-rich, volcanically influenced Algoma-type BIF, whereas Gārsene shows a stronger affinity to a sediment-associated Superior-type BIF. Mineral assemblages record transitional amphibolite–granulite- to low-temperature granulite-facies conditions at Staicele and granulite- to amphibolite-facies retrogression at Gārsene. Magnetite from Staicele contains an average of 3.1 wt.% MnO, and Mn is also hosted by garnet and pyroxene. The Gārsene magnetite quartzites locally contain up to 555 g/t^{-1} Co and elevated Ti and V. Staicele also shows geochemical similarities to the Jõhvi deposit in Estonia and to Fe–Mn systems of the Bergslagen district in Sweden. These results refine the genetic interpretation and resource potential of the Latvian basement iron formations.

Keywords: BIF; Latvian–East Lithuanian block; Magnetite quartzites; Metamorphism; Precambrian

*Corresponding author (email: dmitrijs.vorobjovs@lu.lv)

Editorial handling: Shenghong Yang (email: shenghong.yang@oulu.fi)

1. Introduction

Ferruginous quartzites or banded iron formations (BIF) are metavolcanic or metasedimentary banded rocks containing iron ore minerals with typical content of >15 (typically 20–35) wt.% Fe (Yin et al. 2023), which are widely found in the Precambrian strata. BIFs are characterised by alternating Fe-rich (e.g., magnetite and hematite) and silicate-rich layers and occur widely in Archean–Proterozoic successions (Schopf 1983; Posth et al. 2011). They may preserve geochemical information on depositional and tectonic environments and, where sufficiently enriched in Fe oxides, form economically important iron ores (Trendall 2002; Yin et al. 2023).

BIFs are commonly classified as Algoma-, Superior-, and Neoproterozoic Rapitan-type deposits. Algoma-type BIFs are associated mainly with Archean–Paleoproterozoic volcaniclastic rocks and palaeovolcanic centres, consistent with submarine hydrothermal input (Gross 1980; Gourcerol et al. 2016). Superior-type BIFs occur mainly in Paleoproterozoic–Mesoproterozoic sedimentary successions lacking direct volcanic association and represent chemical precipitation from Fe-rich waters in shallow settings (Johnson et al. 2008).

The presence of iron-rich rocks in Latvia was confirmed from 1920s to 1970s, when magnetic anomalies were found in the north, centre and south of the country (Kuršs & Stinkule 1997), and in the early 1980s, when several boreholes were drilled in potential ore-bearing rocks according to aeromagnetic survey of the territory (Vetrennikov 1984). According to these previous studies – Vetrennikov (1984, 1991), the most promising sites are the Staicele and Gārsene magnetic anomalies.

This study is related to the renewed interest in crystalline basement ores in Latvia and activities in their exploration. The main task of the study is to characterise the types of iron-rich rocks of the Staicele and Gārsene deposits, their mineralogical composition and geochemical features, based on new analyses of previously collected drill cores. The origin of the deposits is discussed as well. The data obtained in this study can be used to assess ore resources in the crystalline basement.

2. Geological setting

The Palaeoproterozoic crystalline basement lies at depths of approximately 300 to 1900 m in the territory of Latvia (Segliņš et al. 2013).

All studied deposits occur as magnetic anomalies within the Latvian–East Lithuanian (LEL) tectonic block (Fig. 1a), which formed during the Svecofennian orogeny between 2.0 and 1.75 Ga (Bogdanova et al. 2015). The accretion of microcontinents and island arcs, followed by the collision of Fennoscandia with the Volgo–Sarmatian microcontinent at approximately 1.82–1.80 Ga, caused intense deformation and metamorphism of the basement rocks. Together with subsequent Proterozoic magmatic activity, these processes formed the crystalline basement beneath Latvia. The LEL block comprises rocks of diverse origins and metamorphic grades and is characterised by N–S-trending magnetic and gravity anomalies. Migmatites are widespread, together with granite, diorite, and gabbro intrusions. Central Latvia contains porphyritic mafic and felsic metavolcanic rocks, metamorphosed clay-rich sedimentary rocks, and associated metamorphosed iron–manganese quartzites (Bogatikov & Birķis 1973; Vetrennikov 1991). Geochronological data for the LEL block in the territory of Latvia remain limited.

The structure of the Staicele deposit (Fig. 1b) was identified by a single borehole Staicele-1 drilled into a magnetic anomaly, with intensity of up to 7150 nT. The borehole intersects the sedimentary cover rocks and then the crystalline basement at the depth of 688–1112.5 metres (Vetrennikov 1984). It was found that the body of ferruginous quartzites occurs among Proterozoic migmatised garnet-biotite and biotite-hypersthene plagiogneisses, more rarely amphibolites (Kuršs & Stinkule 1997) of LEL tectonic block (Bogdanova et al. 2015).

The ore-bearing sequence comprises five bodies, with each 40–50 m thick and a cumulative thickness of 228 m, and barren interlayers up to 40 m thick. Magnetite quartzites constitute ~20 wt.% of the borehole section and contain 46–52 wt.% $Fe_2O_3^t$ and up to 11.5 wt.% Mn (Kuršs & Stinkule 1997). The ore bodies dip steeply (75–80°), generally towards the SW, although the precise dip azimuth remains uncertain (Karušs et al. 2026). Magnetic and gravity forward modelling data suggest the ore-body area of ~35 km^2 and a possible deep extension of 3–13 km related to the anticlinal structure (Vetrennikov 1991; Kuršs & Stinkule 1997; Segliņš et al. 2013).

The Gārsene deposit (Fig. 1b) was discovered in the 1980s (Segliņš et al. 2013). Geophysical studies indicate three iron-ore layers with a total thickness of ~200 m, extending to at least 4.5 km depth. Borehole Subate-2A, drilled at the 9500 nT magnetic anomaly peak, intersected a ~45 m thick layer with an estimated true thickness of ~24 m due to its synclinal structure (Vetrennikov 1984, 1991). The layers dip at a steep angle of 70–80° towards the southwest (Vetrennikov 1991).

The total iron oxide content of Gārsene iron-rich rocks is 20–64 wt.%, while approximately 75 % of the analysed ore samples have total iron oxide contents close to 45 wt.%. The richest quartz-magnetite ores occur in the central part of the ore body, whereas amphibole- and biotite-magnetite ores occur in its lower and upper parts (Kuršs & Stinkule 1997). The resources to depth 1500 m were evaluated as approximately 2.1 billion tonnes, and ca. half of this thickness interval was classified as ore, however the methodology of this evaluation was not described (Brangulis & Straume 1984).

3. Materials and methods

The studied rock material includes 56 samples taken from the borehole Staicele-1 (Staicele deposit: 57.833122° N, 24.740270° E) and 36 samples from the borehole Subate-2A (Gārsene deposit: 56.064284° N, 25.791902° E). They were collected from the Gardene borehole storage facility managed by the Latvian Environment, Geology and Meteorology Centre (LEGMC). Thin sections based on epoxy resin were prepared from 80 selected samples in the Rocks Research Laboratory of the Department of Geology at the Faculty of Science and Technology, the University of Latvia.

Previously prepared thin sections (242 ones from Staicele and 181 from Gārsene deposit) from the State Geological Fund collection of LEGMC were used as well.

Representative portions spanning the full thickness of each sample were cut and crushed for chemical analysis. Scanning electron microscopy (SEM) combined with energy-dispersive X-ray spectroscopy (EDX) was used to determine the chemical composition of individual ore minerals. SEM–EDX analyses of magnetite were also conducted to assess potentially valuable trace-element admixtures. Magnetite, pyrite, pyrrhotite, as well as garnet- and pyroxene-group minerals, from eleven samples from each deposit (S01–S011 and G01–G011; 22 samples in total) were analysed using: (1) surface elemental mapping and (2) single-point analysis of selected inclusions. A Hitachi S-4800 field-emission scanning electron microscope equipped with a Bruker XFlash 5010 EDX detector was used. For Mn, Si, Al, Fe, Ca, and Ti, precision was 0.61–2.76 % CV and absolute bias was 0.04–1.93 %. The analyses were conducted at the Institute of Chemical Physics, University of Latvia.

Inductively coupled plasma mass spectrometry (ICP–MS) was used to analyse powders from 44 Staicele and 24 Gārsene samples. An Agilent 8900 ICP-QQQ mass spectrometer equipped with a MicroMist nebuliser and a helium/hydrogen collision/reaction cell was used at the Faculty of Medicine and Life Sciences, University of Latvia. Trace-element ratios provided information on the genesis of the deposits.

Samples were prepared using microwave-assisted digestion. A mixture of 1 mL concentrated hydrofluoric acid (HF, 48 %, Fisher Scientific, Trace Grade), 3 mL concentrated hydrochloric acid (HCl, 37 %, Fisher Scientific, Trace Grade), and 6 mL

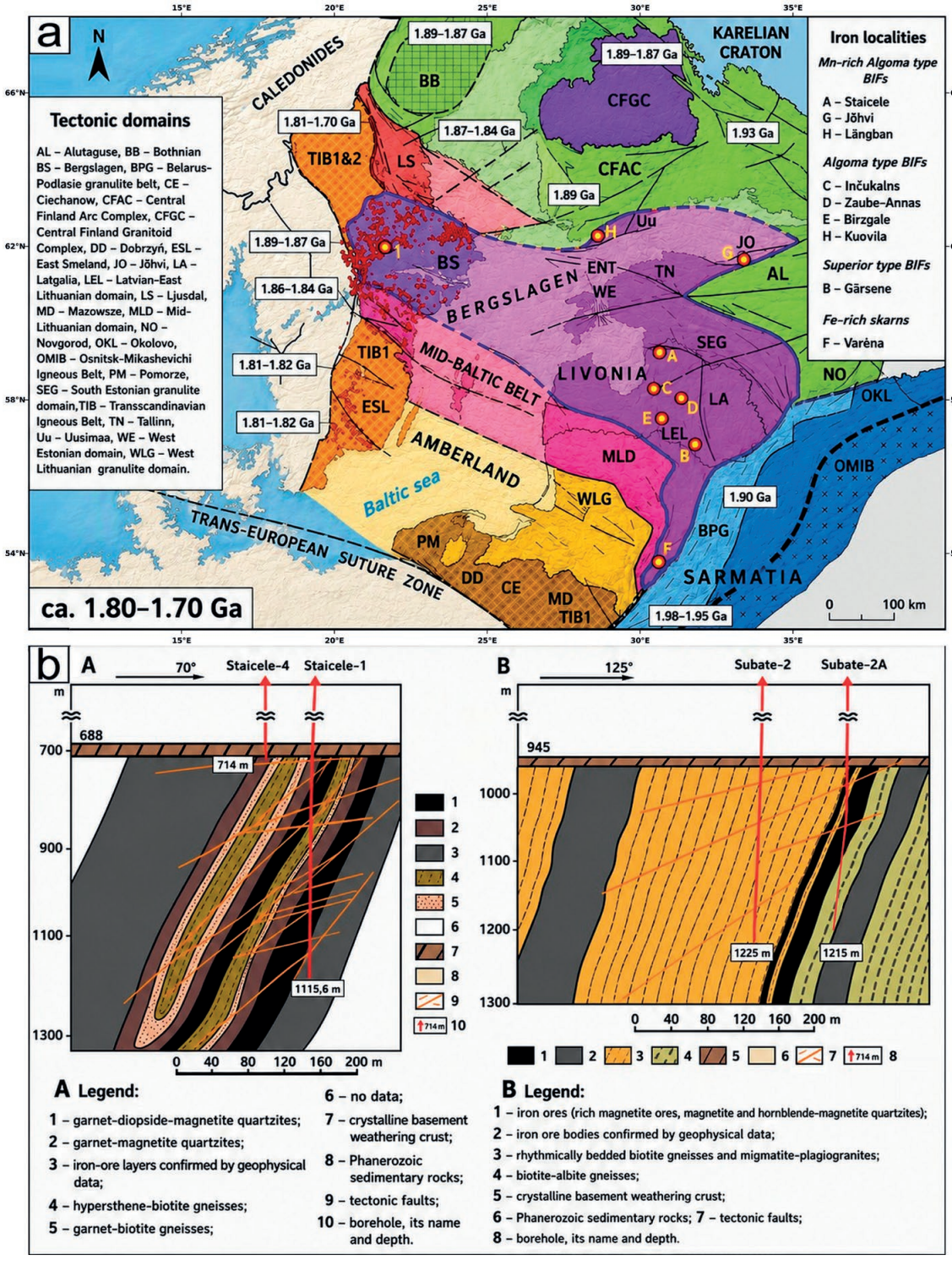


Figure 1. a) Tectonic map of the Fennoscandian paleocontinent after Bogdanova et al. (2015), highlighting the boundaries of tectonic domains and the formation ages of the major tectonic units, with particular emphasis on the Bergslagen-Livonia microcontinent, the distribution of iron ore deposits within it, and the principal clusters of BIF-hosted iron ore and related skarn deposits in the Bergslagen region. b) Geological section of the studied deposits – Staicele (A) and Gārsene (B) based on the drilling and geophysical data after Vetrennikov (1991).

concentrated nitric acid (HNO_3, 65 %, Fisher Scientific, Trace Grade) was added to 0.1 g of each sample. The mixture was digested in a Milestone Start E microwave system at 180 °C for 35 min to ensure complete sample decomposition. The ICP–MS was calibrated using certified solutions traceable to NIST SRMs: 68 Component ICP–MS Standard (High-Purity Standards, 10 mg L^{-1}), Multielement Standard Solution 6 for ICP (Sigma-Aldrich, 100 mg L^{-1}), and ICP Calibration Standard HCl Soluble Elements XVII, 7 components (CPA, 100 mg L^{-1}). ICP–MS performance was assessed using repeated QC measurements at 25 µg L^{-1} (A and B; n = 3) and 0.5 µg L^{-1} (C; n = 2). LOD and LOQ were calculated as 3s and 10s from three blanks. For Ti, V, Mn, Fe, Co, Ni, Cu, Zn, Zr, Y, Nd, Sm, Eu, Gd, Dy, Er, and Yb, CV values were 1.5–3.2 % and absolute deviations ≤3.5 % (Appendix A).

A SHIMADZU EDX-7000 X-ray fluorescence spectrometer equipped with a silicon-drift detector and EDXIR-Analysis software was used for XRF analyses of 44 samples from the Staicele-1 borehole. The following parameters were applied: step, 0.02 keV; anode voltage, 4–50 kV; anode current, 1–1000 µA; 2048 points; acquisition range, 0–40.96 keV; and measurement range, Al–U (180 s) and Na–Sc (40 s), under vacuum. The analyses were conducted at the Latvian Assay Office.

XRF analytical accuracy and precision were assessed by seven replicate analyses of a certified IMS PBS-310 (pulverised sediments and low-grade BIF) reference material. Precision was expressed as relative standard deviation (RSD), and accuracy as relative bias from the certified values. For the major oxides, RSD ranged from 0.15 to 1.79 %, while absolute relative bias was ≤0.49 %. The low-concentration components P_2O_5, SO_3, and BaO showed higher RSD values of 3.10–7.20 % and absolute relative biases of 1.40–4.08 %. The complete quality-control results are provided in Electronic Appendix A.

Magnetite powder was extracted from samples from both deposits for X-ray diffraction (XRD) and XRF analyses to determine the average chemical and mineralogical composition of the iron-rich rocks. Extraction of magnetite is the principal industrial method used to produce iron-ore concentrate (Zhang et al. 2021). Its laboratory-scale application therefore provides an estimate of the composition of a potential concentrate from each deposit.

XRD analyses were used together with polarised-light microscopy to confirm the mineralogical composition of the ores. The analyses were conducted using a Bruker D8 Advance powder diffractometer equipped with a LYNXEYE detector, XRD Commander control software, and EVA 12 data-processing software. The analytical parameters were: step, 0.02°; counting time, 0.1 s; anode voltage, 40 kV; anode current, 40 mA; and scanning range, 5–60°. The analyses were conducted at the Faculty of Medicine and Life Sciences, University of Latvia.

4. Results

4.1. Rock types

The Staicele deposit is characterised by the presence of manganese-bearing ferruginous quartzites (Fig. 2a–c) and a wide development of rocks of medium-felsic composition: garnet-biotite, biotite-hypersthene, and hypersthene-amphibole microgneisses (leptites), which are associated with manganese-bearing garnet-magnetite and garnet-pyroxene-magnetite ferruginous quartzites and rarely amphibolites (Table 1).

Table 1. Petrographic characteristics of the Staicele deposit.

Rock type	Colour	Grain size	Texture	Structure	Main mineral composition (vol.%)	Secondary minerals	Accessory minerals	Remarks
Garnet-biotite gneiss	Pinkish grey	Fine-medium	Granoblastic, lepidoblastic	Banded–massive	Qz 10–50; Pl 5–50; Kfs 10–25; Grt 3–10; Bt 3–15; Mag 1–15	-	Zrn, Ap	Described as leptites by V. Vetrennikov in (Vetrennikov 1984, 1991). Is widely found in the section.
Hypersthene-biotite plagio-microgneiss	Dark grey	Fine	Lepidoblastic, granoblastic	Banded	Pl 40–60; Qz 15–40; Opx 3–15; Bt 3–10; Mag 3–10; Kfs 0–5	-	Zrn, Ap	-
Pyroxene-amphibole (±Bt) gneiss	Greyish green	Fine	Lepidoblastic, granoblastic	Banded	Pl 50–60; Amp 10–20; Px 5–10; Mag 5–10; Bt 1–15; Qz 0–10	-	Ap, Zrn, Ttn	-
Amphibolite	Greenish black	Fine-medium	Lepidoblastic, granoblastic, schistosity	Layered	Amp 20–60; Pl 20–40; Qz 0–20; Px 0–15; Opx 0–18	Chl, Act, Carb	Ap, Zrn	Interlayers 0.02–0.5 m thick, found throughout the section.
Charnockite	Light grey	Medium	Porphyroblastic	Massive	Olg 35–50; Qz 20–35; Kfs 1–15; Bt 0–15; Opx 1–10; Grt 0–10; Mag 1–12	-	Ap, Zrn	Rock of granulite facies.
Magnetite quartzite (MagQ)	Black-grey	Fine-medium	Granoblastic	Banded spotted-embedded	Qz 40–70; Mag 20–40; Px 0–5; Grt 0–5	Hem, Chl, Carb	Ilm, Ap	Main ore type (further in the text – MagQ).
Pyroxene-garnet-magnetite quartzite (PxGrtMagQ)	Dark green, black	Fine-medium	Granoblastic	Banded, spotted-embedded	Qz 5–60; Mag 15–50; Grt 5–40; Px 10–50	Carb, Serp, Chl, Tlc, Hem,	Ilm, Rt, Ap, Zrn, Py	Main ore type (further in the text – PxGrtMagQ).
Biotite-pyroxene-garnet-magnetite quartzite	Dark green, black	Fine-medium	Granoblastic, lepidoblastic,	Banded, spotted-embedded	Qz 5–60; Mag 15–50; Grt 5–40; Px 10–50; Bt 3–8	Carb, Serp, Chl, Tlc, Hem,	Ilm, Rt, Ap, Zrn, Py	Biotite-rich subtype of PxGrtMagQ. It may rarely contain carbonates 30–40 %
Magnetite garnetite	Dark red	Fine-medium	Granoblastic	spotted-embedded	Grt 55–75; Mag 15–30	Carb	Pl	Often the rock form separate strips in banded quartzites.
Magnetite-bearing garnet pyroxenite	Dark green, reddish	Fine-medium	Granoblastic	spotted-embedded	>75 % Grt+Px; Mag,Qz≤10	-	-	High P/T metamorphic rock (Fettes & Desmons 2007), similar to granulites, but of pyroxene-garnet composition.

The Palaeoproterozoic rocks in the ***Gārsene*** deposit consist of biotite and amphibole-biotite microgneisses, amphibolites, and magnetite ferruginous quartzites (Table 2). The rocks often are massive, very rich magnetite ores, frequently with significant sulphide admixture (Fig. 2d–e).

Table 2. Petrographic characteristics of the Gārsene deposit.

Rock type	Colour	Grain size	Texture	Structure	Main mineral composition (vol.%)	Secondary minerals	Accessory minerals	Remarks
Biotite-albite microgneiss	Dark grey	Fine	Granoblastic, lepidoblastic	Banded-massive	Ab 20–70; Qz 10–70; Bt 5–20	Chl, Ep, Carb	Zrn, Ap, Ttn, Mag, Tur, Px	Often migmatised
Secondary granitised gneiss	Dark grey, pink	Medium-coarse	Granoblastic, lepidoblastic	Banded	Pl 30–60; Qz 30–50; Bt 1–10; Kfs 2–5; Mag 1–7	Chl, Hem	Zrn, Ttn	Often migmatised
Migmatite	Dark grey, pink	Medium-coarse	Granoblastic, lepidoblastic	Banded	Paleosome + granite leucosome	-	Zrn, Ttn	-
Amphibolite	Dark	Medium-coarse	Nematoblastic, schistosity	Layered	Amp 35–88; Pl 8–35; Bt 8–20; Qz 0–10	-	Ant, Zrn, Ttn, Ap, Mag	-
Rich magnetite quartzite	Black-white	Medium-coarse	Massive	Massive	Mag 55–95; Qz 5–45; Pyh+Py 5–15	Hem	Amp, Px, Bt, Chl, Mo, Tur, Ap	High-grade ore (further in the text – RMagQ)
Magnetite quartzite	Black-white	Fine-medium	Banded	Banded spotted-embedded	Mag 25–55; Qz 45–75; Pyh+Py 0–15; Amp 0–5	Chl	Bt, Zrn, Amp, Ap	Main ore (further in the text – MagQ)
Amphibole-magnetite quartzite	Black-white, green	Fine-medium	Banded	Banded, spotted-embedded	Mag 30–50; Qz 30–40; Amp 10–40	Hem, Py, Pyh	Ilm, Ap	Silicate-rich ore (further in the text – AmMagQ). Sometimes separate zones of apatite and sulphide mineralisation are found in this type of quartzites.

It should be noted that, in the Subate-2 borehole (Fig. 1b), numerous quartz veins containing large magnetite and amphibole lenses were observed within the biotite-albite microgneisses, secondary granitised gneisses, and migmatites.

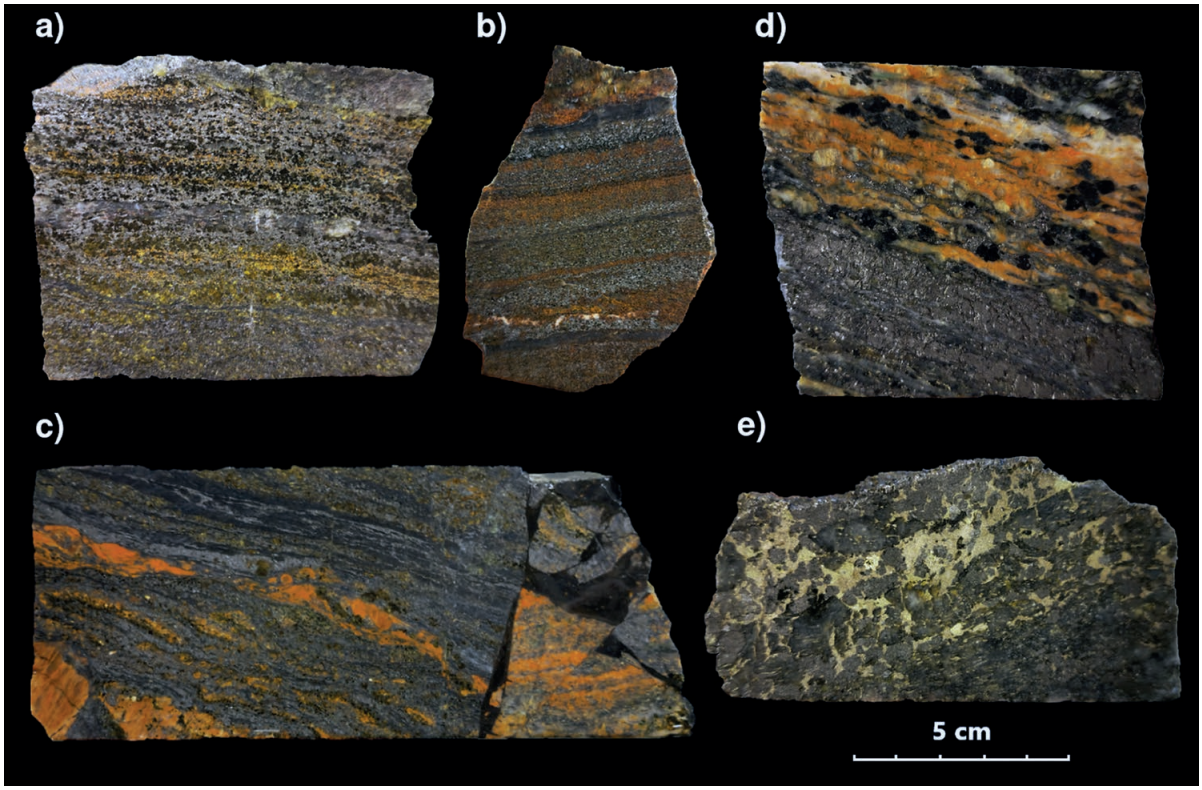


Figure 2. a)–c) Photos of sawed and polished drillcore slabs: banded magnetite quartzites with high content of silicates – typical iron-rich rocks of the Staicele deposit a) banded pyroxene-garnet-magnetite quartzite; Staicele-1 borehole; depth 782.7 m; no. S13; b) banded garnet-pyroxene-magnetite quartzite; Staicele-1 borehole; depth 803.4 m; no. S17; c) banded pyroxene-magnetite-K-feldspar quartzite with untypical zone of fault-breccia manifested in the form of cataclasitation with black pseudotachylyte cement, which indicate dynamic metamorphism; Staicele-1 borehole; depth 1061.95 m; no. S37. d)–e) Iron ores of the Gārsene deposit – massive, with altered primary texture oxide-silicate and oxide-sulphide ores; d) amphibole-magnetite quartzite, consisting of large magnetite and quartz-amphibole bands; Subate-2A borehole; depth 1097.8 m; no. G17; e) rich magnetite quartzite with typical altered structure and high content of sulphides, mainly pyrrhotite (darker) and pyrite (lighter grains); Subate-2A borehole; depth 1100.55 m; no. G19.

4.2. Chemical composition of minerals

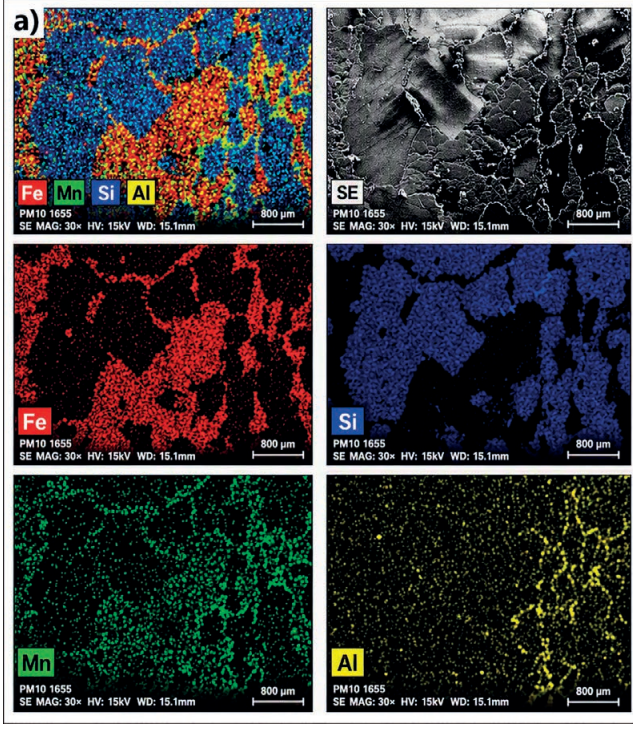
4.2.1. Magnetite

The trace-element composition within the magnetite is relatively uniform: grains of minerals located in opposite parts of the same sample exhibit nearly identical compositions. The magnetite from Staicele has relatively high content of Mn, in turn, the Gārsene samples do not show any increases (Fig. 3 and Fig. 4d–e).

According to the data obtained by SEM-EDX, the even distribution of manganese in the ore samples suggests that this element is part of the magnetite crystal lattice rather than existing as separate mineral inclusions in the magnetite matrix. However, the manganese content of the magnetite varies at different depths, indicating their uneven distribution within the deposit. A more detailed analysis of the existing drill core at a given depth is required to obtain a more accurate result on their content.

4.2.2. Garnet group

The composition of the garnet group minerals at Staicele is complex. In most cases (S01, S07, S011), the garnets are predominantly spessartine, about half of the garnet weight, as indicated by the prevalence of manganese in the composition. The second half of the garnet mass consists of almandine and grossular with a similar ratio and a small admixture of pyrope. The formula based on these samples is calculated as $Sps_{46.5–55.0}Alm_{21.8–}$



b)

Sample no.	Depth interval in borehole (m)	Mn (wt.%)
S01 (1)	747–753	2.11
S01 (2)	747–753	2.10
S04	783–787	3.19
S06	790–794	3.69
S07	794–797	3.67
S08	1069–1071	1.41
S011	1104–1107	1.88
Concentrate*	**all intervals**	**2.46**

S01 (1) and S01 (2) represent different magnetite grains from the same sample.

* The concentrate value represents the mean composition of magnetite separated from 44 Staicele ore samples.

Figure 3. a) Typical elemental distribution observed by SEM-EDX in ores from the Staicele deposit (SE - SEM-EDS photograph without reflectance analysis; Fe - iron distribution on the sample surface, Si - silicon, Mn - manganese, Al - aluminium; Fe, Mn, Mg, Al - combined photograph of iron, manganese and magnesium). Magnetite has an elevated Fe and Mn content. In places high concentrations of Si and Fe, and maximum concentrations of Al and Mn correspond to garnet rims, which surround pyroxene crystals. Si and Mg are simultaneously abundant in pyroxene crystals. Borehole: Staicele-1, depth interval 783–787 m, sample S04. b) Valuable accessory elements detected in magnetite grains in other samples of Staicele deposit by EDS.

$_{25.0}Grs_{16.5–23.3}Prp_{5.4–8.0.}$ The exception is sample S08 – $Grs_{36.1}Alm_{33.0}Sps_{28.7}Prp_{2.3}$ with a close spessartine, almandine, and grossular ratio with a slight predominance of the Grs component. Propagation of SEM–EDX precision and accuracy produced narrow Sps, Alm, and Grs intervals and did not change garnet classification, the same applies to pyroxenes. The mineral chemical data are found in Electronic Appendix A, ternary compositional diagrams in Fig. 4a–b. SEM–EDX accuracy and precision were evaluated by five replicate analyses of a reference material.

4.2.3. Pyroxene group

The composition of the pyroxene group of the Staicele deposit varies considerably. Based on the cationic composition of pyroxenes, almost all samples (except S011 – $Wo_{45.9}En_{30.2}Fs_{24.0}$) are dominated by the enstatite component, with variable proportions of Wo and Fs. The most common case is the basic composition of Mg-Fe in samples S04, S06 (1), S08 (1,2) with the general formula – $En_{69.6–86.9}Fs_{10.9–22.2}Wo_{1.0–6.1}$ and Mg-Ca-Fe pyroxenes – S06 (2), S07 (1,2) with formula $En_{51.7–59.1}Wo_{25.5–29.5}Fs_{15.4–18.8.}$ It should be noted that all pyroxenes contain manganese. In sample S07 the pyroxene grains contain manganese as one of the main components. Almost all the pyroxenes analysed contain small amounts of Na (from 0.34 to 0.94 wt.%) and Al (from 0.45 to 2.33 wt.%) impurities. Based on ternary compositional diagrams (Fig. 4c) five clinopyroxene grains were identified: 1 was classified as pigeonite and 4 as augite. Additionally, 4 orthopyroxene grains were identified as enstatite. The mineral chemical data are found in Electronic Appendix A.

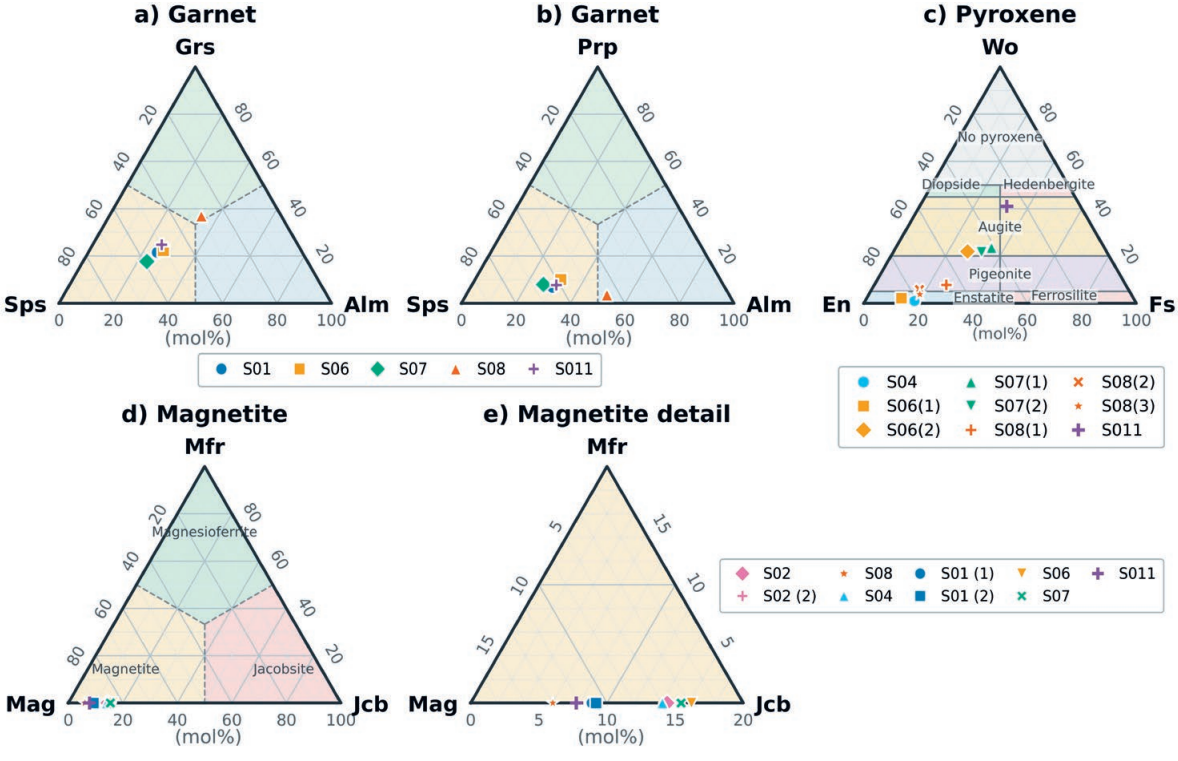


Figure 4. Ternary compositional diagrams of minerals from the Staicele deposit: a) Sps–Alm–Grs and b) Sps–Alm–Prp garnet diagrams; c) Wo–En–Fs pyroxene classification diagram; d) Mag–Jcb–Mfr magnetite diagram; and e) enlarged 0–20 mol% section of the magnetite diagram.

Table 3. Chemical composition of sulphides from the Gārsene iron ore deposit determined by SEM-EDX method, concentrations were normalised to 100 %

Element \ sample	Pale sulphides					Dark sulphides		Standards	
	G03 (1)	G03 (2)	G05	G06	G08	G03	G06	Pyrite	Pyrrhotite
	Mass, wt.%								
Fe^t	56.5	49.8	53.8	50.7	49.0	66.7	74.6	46.6	62.3
S	43.5	50.2	46.2	48.9	51.0	33.3	25.2	53.4	37.7
Cu	b.d.l.	b.d.l.	b.d.l.	0.4	b.d.l.	b.d.l.	0.2	b.d.l.	b.d.l.

(b.d.l. – below detection limit; G03 (1)/(2) – different sulphide grains from the same sample)

4.2.4. Sulphides

The pale and dark sulphides differ in chemical composition (Table 3). The Fe^t and S contents of the pale sulphides are broadly comparable with the pyrite standard, whereas the dark sulphides have higher Fe/S ratios, consistent with pyrrhotite.

The pale sulphides are characterised by Fe/S atomic ratios corresponding approximately to $FeS_{1.34}$–$FeS_{1.81}$ and are therefore interpreted as pyrite. The dark sulphides show Fe/S ratios ranging from $FeS_{0.87}$ to $FeS_{0.59}$, consistent with pyrrhotite, which is also confirmed by XRD analysis. Deviations from ideal stoichiometry are interpreted as the result of fine-scale intergrowths and mineral inclusions within the analysed grains, as well as partial overlap of the EDX interaction volume with neighbouring Fe-rich phases.

4.3. Major elements of ores

The major components of the magnetite ores from the Staicele and Gārsene deposits are presented in the Electronic Appendix A.

The average $Fe_2O_3^t$ content of silicate-poor Staicele ores is similar to that of Gārsene AmMagQ and MagQ (~42–44 wt.%; Table 4), whereas silicate-rich PxGrtMagQ has a lower average of 31.4 wt.% and Gārsene RMagQ shows the highest values. Staicele ores are Mn-rich, with mean MnO contents of 3.97–5.87 wt.%, whereas MnO is nearly absent at Gārsene; magnetite from 44 Staicele samples averages 3.1 wt.% MnO. Al_2O_3, TiO_2, MgO, CaO, and K_2O are highest in silicate-rich PxGrtMagQ and AmMagQ and lower in MagQ, while Na_2O is absent from the analysed ores. SO_3 and P_2O_5 are lower at Staicele, whereas the highest S contents occur in Gārsene RMagQ.

The XRF quality-control results indicate low analytical uncertainty relative to the overall Fe–Mn compositional differences observed between the deposits. Relative biases were –0.048 % for $Fe_2O_3^t$ and –0.064 % for MnO. Higher relative uncertainties were observed for P_2O_5 and SO_3 because of their low concentrations. The complete quality-control results are provided in Electronic Appendix A.

4.4. Trace elements of ores

The Staicele and Gārsene ores show distinct trace-element compositions (Fig. 5). Ti averages 1221, 766, and 272 ppm in Gārsene AmMagQ, MagQ, and RMagQ, respectively, compared with 1037 and 443 ppm in Staicele PxGrtMagQ and MagQ. Gārsene is enriched in V, Co, Cu, Ga, and Ni, whereas both deposits show similar Pb, U, Hf, Cr, and Zr concentrations. Co averages 137, 254, and 436 ppm in Gārsene AmMagQ, MagQ, and RMagQ, respectively; sulphide-rich samples (9 of 24) contain 217–999 ppm Co (average 555 ppm). In contrast, Staicele PxGrtMagQ and MagQ average 60.5 and 50.7 ppm Co, respectively, but are enriched in Zn (~96 ppm). The other results of representative samples can be seen in Electronic Appendix A.

Table 4. Chemical composition of different ore types from Staicele and Gārsene iron ore deposits determined by XRF method.

Oxide	Staicele deposit				Gārsene deposit					
	MagQ		PxGrtMagQ		AmMagQ		MagQ		RMagQ	
	Range, wt.%	Mean, wt.%	Range, wt.%	Mean, wt.%	Range, wt.%	Mean, wt.%	Range, wt.%	Mean, wt.%	Range, wt.%	Mean, wt.%
$Fe_2O_3^t$	30.6–59.1	41.7	13.3–47.9	31.4	20.7–58.4	43.7	26.3–56.1	41.8	58.2–92.6	76.5
MnO	1.17–8.29	3.97	1.47–18.9	5.87	0–0.04	0.03	0–0.02	0.02	0–0.04	0.02
SiO2	17.1 -58.9	46.4	33.5–64.3	48.5	15.3–56.7	40.1	39.8–62.7	51.6	3.84–36.4	15.8
Al_2O_3	0–1.67	0.93	1.08–10.9	4.25	1.35–10.0	4.44	0.26–5.79	1.51	0.23–3.50	1.44
TiO_2	0–0.59	0.10	0–0.76	0.20	0–1.18	0.25	0–0.79	0.10	0–0	0
MgO	0–4.61	2.80	1.32–16.6	5.26	2.98–7.23	4.44	0–2.28	0.80	0–5.42	1.30
CaO	1.00–4.92	2.37	0.84–6.71	4.05	0.49–9.35	2.62	0.19–2.85	1.35	0.35–0.97	0.64
K_2O	0–0.14	0.03	0–2.89	0.42	0.08–1.78	0.70	0–0.33	0.10	0–1.01	0.23
SO_3	0–0.16	0.07	0–0.19	0.06	0.91–4.62	1.90	0.50–3.22	1.30	0.67–5.75	3.14
P_2O_5	0–0.84	0.29	0–1.36	0.21	0.08–8.21	1.75	0–4.11	1.34	0.26–1.39	0.69

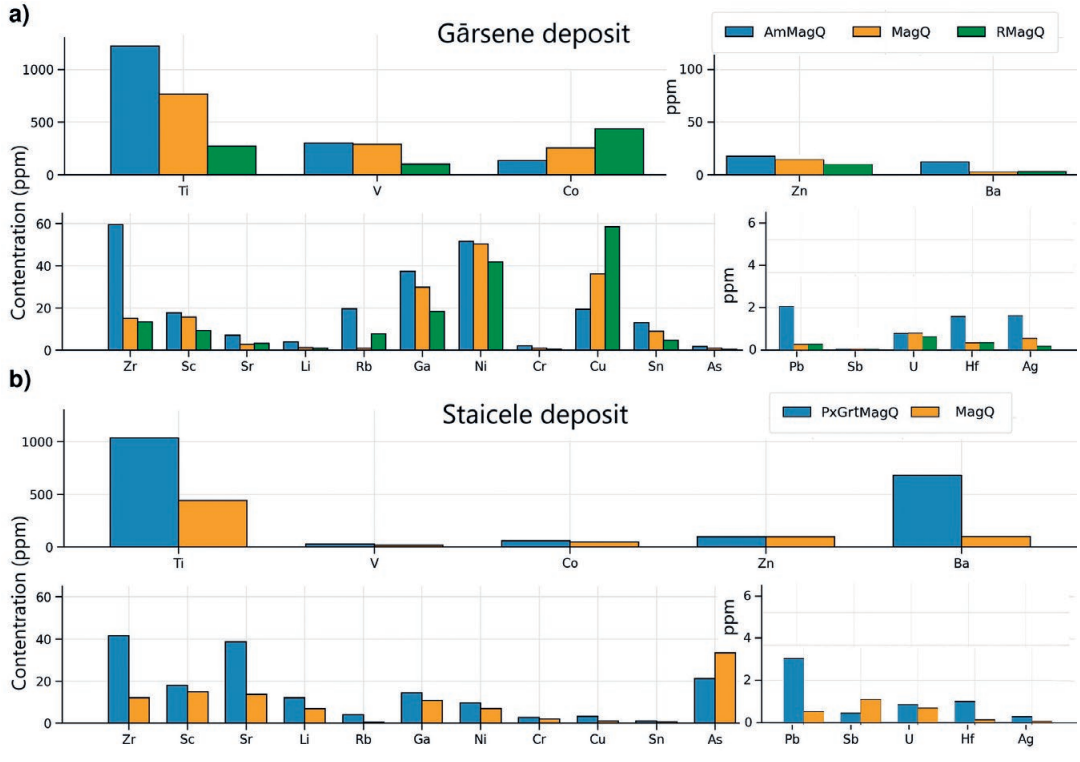


Figure 5. Mean concentrations of selected trace elements in the a) Gārsene ore types (AmMagQ, MagQ, and RMagQ) and b) Staicele ore types (PxGrtMagQ and MagQ). Analytical uncertainty is substantially smaller than the observed differences among ore types; therefore, the principal trace-element trends remain valid.

At Staicele, ∑REE concentrations in PxGrtMagQ and MagQ, excluding feldspar-bearing samples, range from 28.4 to 148 ppm (average 80.2 ppm), nearly twice the Gārsene average of 41.9 ppm (5.76–114 ppm). Secondarily granitised Gārsene quartzites reach ∑REY values of up to 464 ppm, likely reflecting feldspar-related enrichment, and were therefore excluded from the geochemical dataset (Electronic Appendix A).

In the case of the Staicele deposit, the Y/Ho ratio varies between 26.2 and 41.3, with an average value of 33.4. The average $(Nd/Yb)_{SN}$ (normalized to Post-Archaean Australian Shale (PAAS); McLennan 1989) ratio in the ores is 3.80, ranging from 1.12 to 9.63. The values of $(Pr/Yb)_{SN}$ and $(Sm/Yb)_{SN}$ are 4.61 (1.26–12.92) and 2.34 (0.89–4.85), respectively. The average LREE/HREE ratio in the Staicele deposit is 5.38 (ranging from 1.33 to 9.17). In turn, the ores of the Gārsene deposit have a Y/Ho ratio of 21.8 (16.00 – 29.4), which is significantly lower, while the $(Nd/Yb)_{SN}$ ratio varies from 1.21 to 5.88, with an average of 2.64. $(Pr/Yb)_{SN}$ 2.76 (1.13 – 6.28), $(Sm/Yb)_{SN}$ - 2.67 (1.13 – 6.28). The LREE/HREE ratio in the Gārsene ores is 2.31 - ranges from 0.99 to 3.40. The average values of these indicators are very similar and, compared to the previous ones, are also high.

The average geochemical coefficient of $(Y/Ho)_{SN}$ for Staicele is 1.23 (ranging from 1.05 to 1.52), while for Gārsene it is 0.80 (ranging from 0.59 to 1.08), further supporting the interpretation of hydrothermal influence in the Staicele deposit and its relative absence in Gārsene.

The average Eu/Eu* PAAS value for the Staicele deposit is 1.26, but in Gārsene more than a third less - 0.73. The proportions remain roughly the same in the case of the yttrium anomaly – in first case, Y/Y* PAAS value is 1.23, in second – 0.75. The following cerium anomaly values were obtained. At Staicele, Ce/Ce* PAAS is slightly higher at 1.1, compared to 1.0 at Gārsene.

After bias adjustment, the mean Ce/Ce*, Y/Y*, Eu/Eu*, Y/Ho, and $(Y/Ho)_{SN}$ values are 1.16, 1.35, 1.29, 40.63, and 1.49, respectively, at Staicele, and 1.06, 0.81, 0.75, 26.49, and 0.97, respectively, at Gārsene. Mean $(Nd/Yb)_{SN}$, $(Pr/Yb)_{SN}$, $(Sm/Yb)_{SN}$, and LREE/HREE ratios are 3.75, 3.74, 2.32, and 5.42 for Staicele and 2.57, 2.22, 2.62, and 2.25 for Gārsene. Thus, Staicele ores retain positive Eu and Y anomalies, elevated Y/Ho values, and pronounced LREE enrichment, whereas Gārsene ores retain negative Eu and Y anomalies, lower Y/Ho values, and weaker overall LREE enrichment.

5. Discussion

5.1. Metamorphic condition of the ores

The iron-rich rocks of the Staicele deposit are characterised by the Cpx–Opx–Pl–Grt–Qz assemblage. Most analysed pyroxenes are clinopyroxenes, previously classified as diopside (Vetrennikov 1984), although their Mg–Fe–Ca compositions deviate from the typical augite series and contain considerable Mn due to isomorphic substitution (Deer et al. 1992). Johannsenite – $CaMn^{2+}Si_2O_6$ and kanoite – $Mn^{2+}(Mg,Mn^{2+})Si_2O_6$ components may therefore occur in their solid solutions (Prewitt 2018). The garnets are also Mn-rich, with dominant spessartine and subordinate almandine–grossular components, whereas the pyrope component is minor (Walters 2022; Wang et al. 2021). The Cpx–Opx–Pl–Grt–Qz assemblage is typical of granulite-facies conditions of approximately 700–900 °C and 800–1200 MPa (Philpotts & Ague 2009). In the amphibolite interlayers, pyroxene and plagioclase are closely associated with amphibole and may represent products of its partial breakdown during prograde metamorphism. Pigeonite with minimum conditions of formation: 800–900 °C and 0.4–1.0 GPa in the BIF supports high-temperature granulite-facies metamorphism, as it is unstable at lower temperatures and transforms into orthopyroxene–augite intergrowths (Borromeo et al. 2023). Although biotite and minor amphibole-bearing interlayers may indicate amphibolite-facies conditions, biotite can persist into the early stages of granulite-facies metamorphism (Indares &

Martignole 1985). Thus, the mineral assemblages of the Staicele ores are typical of transitional amphibolite–granulite-facies or low-temperature granulite-facies conditions.

According to the mineralogical paragenesis, the iron-rich rocks of the Gārsene deposit are characterised by the association Amp–Pl–Qz±Bt, which is typical of amphibolite-facies metamorphism (Philpotts & Ague 2009). However, relict pyroxene inclusions and amphibole pseudomorphs after pyroxene indicate an earlier, higher-grade metamorphic stage. Amphiboles generally form euhedral crystals that are larger than the pyroxenes and therefore appear to have crystallised later. These textural relationships are typical of the retrograde replacement of a granulite-facies assemblage under amphibolite-facies conditions. Thus, the present mineral assemblage of the Gārsene ores is characteristic of transitional granulite–amphibolite-facies conditions.

5.2. Ore quality

Total iron-rich rocks of the Staicele deposit have $Fe_2O_3^t$ content ranging from 13.3 to 59.1 wt.%, correspond to approximately 9.3–41.3 wt.% total Fe, classifying the studied rocks predominantly as low-grade iron ore or ferruginous protore (Clout & Simonson 2005). Magnetite is the main iron-bearing mineral, although garnet and pyroxene also host considerable Fe in PxGrtMagQ. MagQ lacking garnet and pyroxene contains 30.6–59.1 wt.% $Fe_2O_3^t$, whereas the lower values in PxGrtMagQ reflect dilution by silicate minerals. Bulk MnO contents range from 1.17 to 18.9 wt.% and average 3.97 wt.% in MagQ. Magnetite contains an average of 3.1 wt.% MnO, with relatively uniform compositions within individual samples but systematic variations with depth (Fig. 3). The ores of the deposit are also characterised by low sulphur and moderate phosphorus contents (Muwanguzi et al. 2012). More extensive sampling, particularly of high-grade intervals, is required for a robust ore-grade assessment, as the current dataset may not fully represent the bulk ore grade, which should be reassessed through more extensive sampling of both low- and high-grade intervals.

At the Gārsene deposit, the $Fe_2O_3^t$ content of the iron-rich rocks is 20.7–92.6 wt.%. The highest concentrations, in average 76.5 wt.%, are in RMagQ. The maximum $Fe_2O_3^t$ concentration corresponds to approximately 64.8 wt.% Fe, thus the richest samples correspond to medium- to high-grade iron-ore range (Muwanguzi et al. 2012). A substantial proportion of the Gārsene RMagQ and MagQ ores are rich in pyrrhotite and pyrite (Table 3; Fig. 5). These sulphide-bearing ores have elevated amounts of Ti, V, and particularly Co, consistent with our previous observations (Ganeev et al. 2024). The analysed sulphide-rich ores contain up to 555 g/t^{-1} Co, indicating significant Co enrichment compared with typical parameters of BIFs. The iron ores are also classified as high-sulphur and high-phosphorus ones according to the criteria of Muwanguzi et al. (2012), and the analytical uncertainties of P_2O_5 and SO_3 do not affect this classification.

5.3. Source of Ti, V, and Co in the Gārsene deposit

The ores are enriched in Ti, V, and Co, previously attributed to submarine volcanism (Vetrennikov 1984; Kuršs & Stinkule 1997). However, their distribution among different ore types suggests element-specific controls rather than a constant hydrothermal input during sedimentation stage. Ti is the highest in AmMagQ, lower in MagQ, and lowest in RMagQ, whereas V is distributed more evenly between AmMagQ and MagQ but is also depleted in RMagQ (Fig. 5). Ti was probably supplied partly by continental silicates and may have been subsequently redistributed into magnetite and other Fe–Ti oxide phases during retrograde metamorphism (Shi et al. 2024). Vanadium may have accompanied siliciclastic material and subsequently adsorbed as V^{5+} into iron-bearing minerals (Dreher et al. 2021).

Cobalt shows the opposite pattern, being enriched with Cu in part of the magnetite- and sulphide-rich RMagQ ores. Recrystallised sulphides, secondary pyrite, granitisation, migmatite relics, and magnetite–amphibole-bearing quartz veins in

borehole Subate-2 (see Fig. 1b), together with weak $\delta^{34}S$ fractionation suggest a relatively homogeneous sulphur source (Vetrennikov 1991). This indicates that the secondary Co-rich pyrrhotite–pyrite mineralisation formed through fluid-assisted sulphide remobilisation and sulfidation during retrograde metamorphism (Craig & Vokes 1993; Qian et al. 2011; Zaronikola et al. 2023). Nevertheless, the Ti, V, and Co enrichment was controlled by changing depositional conditions, mineral affinity, and subsequent metamorphic redistribution.

5.4. Ore genesis

5.4.1. Continental input into BIF systems

To estimate the terrigenous contribution, the mean Al_2O_3, Ti, and Zr concentrations were normalised to PAAS. These relatively immobile components are commonly associated with detrital aluminosilicates and accessory minerals and can therefore be used to evaluate siliciclastic contamination in BIFs (McLennan 1989; Gourcerol et al. 2016). The resulting values were averaged to obtain a first-order PAAS-equivalent estimate for each ore type (Table 5).

PAAS-equivalent estimates based on mean Al_2O_3, Ti, and Zr concentrations indicate moderate siliciclastic contributions to Staicele PxGrtMagQ (19.9 %) and Gārsene AmMagQ (24.2 %), whereas Staicele MagQ, Gārsene MagQ, and RMagQ show only minor contributions of 6.1 %, 8.3 %, and 5.8 %, respectively. Minor bias adjustments to Ti (+3.4 %) and Zr (+1.7 %) do not affect the estimated siliciclastic contribution, which remains the highest in Staicele PxGrtMagQ and Gārsene AmMagQ (McLennan 1989; Gourcerol et al. 2016). Higher $(Nd/Yb)_{SN}$, $(Pr/Yb)_{SN}$, and LREE/HREE (Section 4.4) ratios at Staicele, together with broadly comparable $(Sm/Yb)_{SN}$ values, indicate a stronger influence of continental material on its REY distribution. Mean $(Y/Ho)_{SN}$ values indicate better preservation of marine Y/Ho fractionation at Staicele, whereas Gārsene generally shows lower Y/Ho and weaker LREE enrichment. The relatively high Ti-based estimate for Gārsene MagQ may reflect Ti hosted in Fe–Ti oxides. These PAAS-equivalent values are semiquantitative indices rather than exact modal proportions (McLennan 1989; Gourcerol et al. 2016; Alexander et al. 2008).

The Al_2O_3/ TiO_2 ratios vary from 7.61 to 79.8 at Staicele (mean 28.8) and from 5.41 to 93.16 at Gārsene (mean 35.49). The mean values are

Table 5. Al_2O_3, Ti, and Zr concentrations and estimated terrigenous contribution to the Staicele and Gārsene iron-rich rocks.

Deposit	Rock type	Element	Range (mean)	Estimated contribution
Staicele	MagQ	Al_2O_3 (wt.%)	0–1.67 (0.93)	6.1 %
		Ti (ppm)	88.2–1257 (443)	
		Zr (ppm)	1.81–39.5 (12.1)	
Staicele	PxGrtMagQ	Al_2O_3 (wt.%)	1.08–10.9 (4.25)	19.9 %
		Ti (ppm)	159–3213 (1036)	
		Zr (ppm)	4.60–110 (41.5)	
Gārsene	AmMagQ	Al_2O_3 (wt.%)	1.35–10.0 (4.44)	24.2 %
		Ti (ppm)	320–3766 (1221)	
		Zr (ppm)	5.80–186 (59.6)	
Gārsene	MagQ	Al_2O_3 (wt.%)	0.26–2.04 (0.89)	8.3 %
		Ti (ppm)	128–3698 (766)	
		Zr (ppm)	<0.05–50.7 (15.1)	
Gārsene	RMagQ	Al_2O_3 (wt.%)	0.30–1.99 (1.22)	5.8 %
		Ti (ppm)	24.1–408 (272)	
		Zr (ppm)	0.49–45.2 (13.4)	

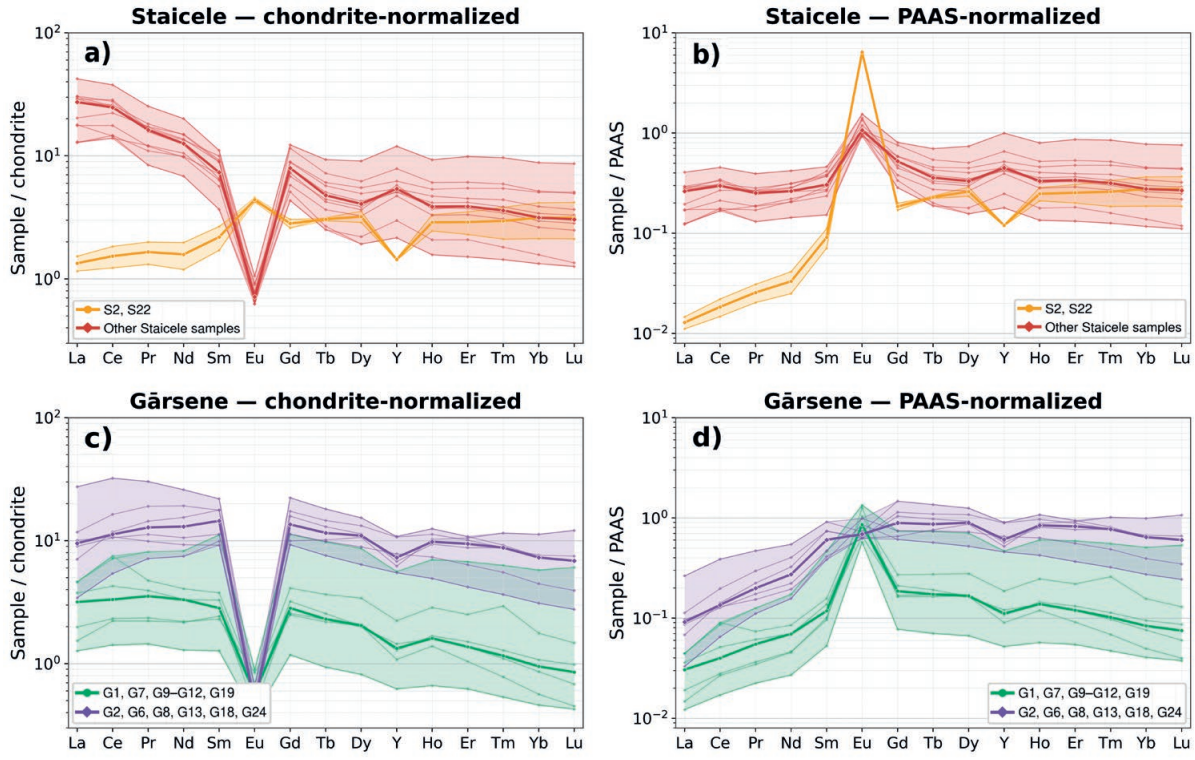


Figure 6. a), c) Chondrite-normalised and b), d) PAAS-normalised REY patterns of ore samples from the Staicele and Gārsene deposits. Bold lines show group medians. Normalising values are from McLennan (1989).

consistent with predominantly felsic provenance 21–70 (Hadji et al. 2024), although the wide ranges indicate variable contributions from mafic, intermediate, and felsic source rocks. Gārsene displays a slightly stronger average felsic signature, whereas both deposits record compositionally heterogeneous or mixed terrigenous sources. Values above 70 may reflect very low Ti contents or mineral sorting and should be interpreted cautiously (Greber & Dauphas 2019).

5.4.2. Palaeoenvironmental conditions of BIF deposition

At Gārsene, AmMagQ and MagQ have broadly comparable REY concentrations, whereas magnetite-rich RMagQ is the most depleted. This pattern is consistent with dilution by REY-poor magnetite and redistribution of REY-bearing accessory and silicate phases during recrystallisation (Alibert 2016; Muhling et al. 2023). The subdued chondrite-normalised patterns and weaker LREE/HREE fractionation at Gārsene further distinguish it from Staicele. At Staicele, the lower REY contents of MagQ relative to PxGrtMagQ probably reflect the greater abundance of garnet, pyroxene, and accessory minerals, together with a stronger detrital contribution to the latter. Thus, REY abundances in both deposits were controlled partly by mineral proportions rather than solely by the composition of the precipitating fluid.

Non-granitised Staicele ores show weakly positive PAAS-normalised Eu and Y anomalies (mean Eu/Eu* = 1.26; Y/Y* = 1.23), consistent with limited high-temperature hydrothermal input and partial preservation of seawater-like Y–Ho fractionation (Bau & Dulski 1996; Planavsky et al. 2010; Muhling et al. 2023). The Eu anomaly occurs in both PxGrtMagQ and MagQ, indicating that it

was not restricted to the silicate-rich lithology. Their $(Y/Ho)_{SN}$ values of 1.05–1.52 support seawater–hydrothermal mixing. In contrast, the negative Eu and Y anomalies and lower $(Y/Ho)_{SN}$ values at Gārsene indicate that this signature was weaker or more strongly attenuated by detrital input and post-depositional redistribution, rather than proving a complete absence of hydrothermal influence (Ernst & Bau 2021; Russo et al. 2024; Yoshida et al. 2024).

Mean Ce/Ce* values of 1.1 at Staicele and 1.0 at Gārsene show no pronounced negative Ce anomalies and thus provide no unambiguous redox constraint. They are compatible with oxygen-depleted depositional waters, but the inverse Ce/Ce*–Pr/Pr* correlations indicate mathematical coupling and require the Ce anomalies to be interpreted together with the complete REY patterns (German & Elderfield 1990; Ohta & Kawabe 2001; Tostevin et al. 2016; Cao et al. 2022).

Bias adjustment preserves the main geochemical distinction between the deposits. Staicele retains higher Eu/Eu*, Y/Y*, Y/Ho, $(Nd/Yb)_{SN}$, $(Pr/Yb)_{SN}$, and LREE/HREE values, whereas Gārsene shows weaker marine Y fractionation and predominantly negative Eu and Y anomalies. However, $(Sm/Yb)_{SN}$ is similar in both deposits and should not be considered as evidence for stronger LREE enrichment at Staicele. The Ce/Ce* values close to unity are insufficient on their own to determine the depositional redox conditions (Bau & Dulski 1996).

According to Conn et al. (2019), the Co/Zn ratio distinguishes hydrothermal (mean ≈ 0.15) from hydrogenetic (mean ≈ 2.5) Fe deposits rather than defining the entire interval as hydrothermal. The Staicele values of 0.17–1.26 (mean 0.67) are consistent with a hydrothermal contribution (Li et al. 2022; Tamehe et al. 2024). In contrast, the extreme Gārsene values of 2.09–218.53 (mean 39.81) lie outside this classification and reflect secondary Co enrichment in pyrrhotite-pyrite mineralisation during metamorphism.

The average PAAS-normalised REY pattern of Staicele resembles that of Jõhvi in its low REY abundance and positive Eu anomaly (Fig. 7). The slightly stronger apparent Ce anomaly at Staicele is not treated as an independent difference because of its inverse relationship with Pr/Pr*. The Sjögruvan Fe–Mn ores in Bergslagen likewise show low REY contents and a pronounced positive Eu anomaly, consistent with hydrothermal–exhalative mineralisation in an arc or back-arc related setting (Frietsch 1982; Allen et al. 1996). These similarities support comparable seawater–hydrothermal contributions and a possible metallogenic link within the Bergslagen–Livonia domain (Beunk & Kuipers 2012; Bogdanova et al. 2015; Soesoo et al. 2021). The negative Eu and Y anomalies and more variable patterns at Gārsene instead indicate stronger modification of the primary REY signature.

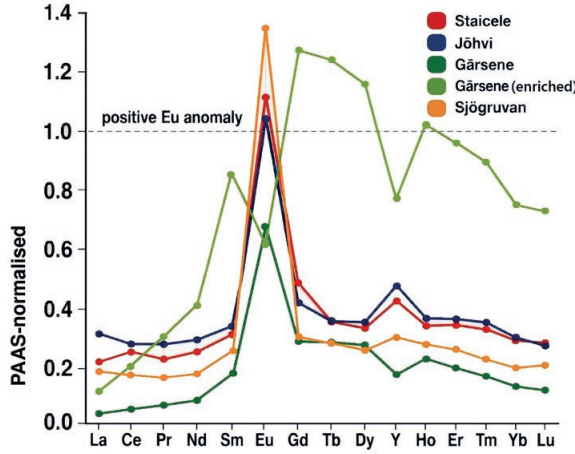


Figure 7. Average PAAS-normalised after McLennan (1989) REE values for the Staicele and Gārsene deposits (Latvia), the Jõhvi deposit (Estonia) after Soesoo et al. (2021), and the Sjögruvan Långban-type deposit quartzites of the Bergslagen area, Sweden, after Holtstam & Mansfeld (2001). A non-logarithmic graph was chosen to allow for a more detailed comparison.

5.4.3. Assessment of geochemical correlations

Regression analyses of the log-transformed indices are presented in Electronic Appendix A. At Staicele, the strong correlation between log(Fe/Al) and log(Fe/Ti) ($r = 0.77$, $p < 0.001$) is consistent with variations in chemical Fe enrichment relative to detrital material (Bau & Dulski 1996; Alexander et al. 2008; Bekker et al. 2010). Because both ratios share Fe in the numerator, however, this relationship

is partly affected by mathematical coupling and is not independent evidence of detrital dilution. Moderate relationships of log(Eu/Eu*) with log(Fe/Al) (r = –0.43) and log(Mn/Fe) (r = 0.39) indicate that the Eu anomaly was also influenced by fluid composition and depositional conditions (Bau & Möller 1993; Danielson et al. 1992). The positive log(Y/Ho)–log(Fe/Ti) relationship and relatively stable Y/Ho and Zr/Hf values are consistent with better preservation of the marine REY signature in Fe-rich samples and limited redistribution of relatively immobile elements (Bolhar et al. 2004). The inverse Ce/Ce*–Pr/Pr* relationship further confirms that Ce anomalies must be interpreted cautiously.

At Gārsene, regressions were evaluated for the complete dataset and for eight samples with nearly identical PAAS-normalised REY patterns. Eu/Eu* and Mn/Fe show little correlation with Fe-enrichment indices, and the REY-stable subset shows no significant relationships between Fe enrichment and REY anomalies; for example, Eu/Eu* correlates neither with Fe/Al (r = –0.34, p = 0.41) nor with Mn/Fe (r = 0.26, p = 0.53). Although the small subset requires caution, the results are consistent with retention of a broadly common REY pattern despite variable ore grade, silica removal, and local alteration. Comparable studies from Carajás, Brazil, and the Sirsi Shelf of the Dharwar Craton, India, show that BIF upgrading does not necessarily erase primary REY patterns, although later fluid alteration may modify Ce anomalies (Justo et al. 2020; Basu et al. 2022).

5.4.4. Summary of ore genesis

The geological, petrographic, and geochemical data indicate that Staicele is a metamorphosed, volcanically influenced BIF deposited in a marine basin receiving limited hydrothermal input and compositionally variable continental material (Bekker et al. 2010; Gourcerol et al. 2016). The REY data preserve evidence of mixing between seawater and hydrothermal fluid, but their generally low abundances do not require exceptionally REE-rich fluids. Elevated LREE/HREE, $(Nd/Yb)_{SN}$, and $(Pr/Yb)_{SN}$ ratios and PAAS-equivalent siliciclastic estimates of 19.9 % for PxGrtMagQ and 6.1 % for MagQ demonstrate stronger continental input into the silicate-rich ores (McLennan 1989; Alexander et al. 2008; Gourcerol et al. 2016).

The studied Proterozoic succession of the Staicele-1 borehole is 428 m thick. Ore layers, 0.2 to 40–50 m thick, alternate with barren gneiss intervals, up to 90 m thick. The gneisses include rocks historically described as leptites and interpreted as metamorphosed felsic volcanic rocks (Vetrennikov 1984, 1991). The layered structure and the occurrence of amphibolites within the ore-bearing succession are consistent with episodic chemical sedimentation interrupted by siliciclastic and volcaniclastic influx, although later deformation and metamorphism probably have modified the original thicknesses. Primary Fe–Mn oxyhydroxide- and silica-rich sediments were subsequently metamorphosed under transitional amphibolite–granulite- to low-temperature granulite-facies conditions into Mn-bearing magnetite, pyroxene, and spessartine–almandine garnet assemblages (Indares & Martignole 1985; Philpotts & Ague 2009). Staicele is therefore most consistent with a metamorphosed Algoma-type BIF formed in a volcanically influenced arc or back-arc marine basin (Allen et al. 1996; Bekker et al. 2010; Gourcerol et al. 2016).

Gārsene is interpreted as a strongly metamorphosed sedimentary BIF formed in a shelf or marginal-marine basin with episodic siliciclastic input. PAAS-equivalent estimates are moderate for AmMagQ (24.2 %) but minor for MagQ (8.3 %) and RMagQ (5.8 %), consistent with the occurrence of silicate-rich AmMagQ within the magnetite-quartzite succession and with the metasedimentary host-rock association (Vetrennikov 1984; McLennan 1989; Gourcerol et al. 2016). Its REY patterns lack a consistently preserved signature of high-temperature hydrothermal fluid, although a hydrothermal contribution to Fe deposition cannot be excluded (Bau & Dulski 1996; Planavsky et al. 2010).

Relict pyroxene and its replacement by larger, later amphibole record an early granulite-facies

stage followed by amphibolite-facies retrogression. Silica removal, magnetite recrystallisation, and fluid-assisted remobilisation of Co–Cu-bearing pyrrhotite–pyrite subsequently modified and locally upgraded the ores. Secondary pyrite generations, granitisation, migmatite relics, and magnetite–amphibole quartz veins in Subate-2 borehole (Fig. 1) support this interpretation, whereas weak $\delta^{34}S$ fractionation is consistent with a relatively homogeneous sulphur source (Vetrennikov 1991). The sedimentary host-rock association – paragneisses including leptites of clastic-sedimentary origin (Vetrennikov 1984), variable siliciclastic input, and lack of a consistently preserved high-temperature hydrothermal signature suggest a closer affinity to sediment-associated Superior-type rather than volcanically associated Algoma-type BIFs (Bekker et al. 2010; Gourcerol et al. 2016).

5.4.5. Regional correlation with Bergslagen, Sweden

The Latvian–East Lithuanian (LEL) domain contains Palaeoproterozoic metavolcanic and metasedimentary rocks associated with Fe–Mn-rich quartzites. A metarhyodacite from northern Latvia was dated at 1870 ± 13 Ma and records granulite-facies metamorphism at 1810 ± 2 Ma. The broadly coeval sedimentation, felsic magmatism, Fe–S–Si mineralisation, and similar crustal evolution support a possible correlation between the LEL/Livonia and Bergslagen domains (Bogdanova et al. 2015).

The Bergslagen volcano-sedimentary succession formed at approximately 1.91–1.89 Ga in an extensional continental-margin or back-arc basin (Allen et al. 1996; Beunk & Kuipers 2012). Swedish Mn-rich iron formations, including Sjögruvan and Gåsborn, are interpreted as exhalative–sedimentary deposits formed by mixing of hydrothermal fluids with seawater. Changes in redox and pH conditions controlled separated Fe–Mn mineralisation, whereas subsequent metamorphism produced the present oxide- and Mn-silicate assemblages (Damman 1988; Holtstam & Mansfeld 2001).

Staicele shows the closest similarity to these Bergslagen Fe–Mn systems**.** Its Mn-rich Fe–Si composition, positive Eu and Y anomalies, association with felsic metavolcanic rocks and amphibolites, and alternation of ore bodies with barren leptite interlayers indicate episodic volcanogenic–hydrothermal activity accompanied by variable siliciclastic input. Granulite-facies metamorphism subsequently redistributed Mn into garnet, pyroxene, and magnetite. Staicele and Jõhvi may therefore represent a metamorphosed exhalative–sedimentary Fe–Mn formation genetically comparable, although not identical, to the Långban-type deposits in Bergslagen.

In contrast, Gārsene may thus represent a more sediment-dominated part of the regional basin system, with a tentative Superior-type affinity. Nevertheless, correlations with Bergslagen remain provisional until the age of ore-bearing rocks in the Proterozoic of Latvia is more precisely constrained. Geochronological data for the crystalline basement of Latvia are still limited, although the reliable ages currently available for the LEL structure are broadly comparable to those reported from the Bergslagen region.

6. Conclusions

The Staicele ores represent a Mn-rich metamorphosed chemical iron formation distinguished by Mn-bearing magnetite, pyroxene, and spessartine–almandine garnet. Their $Fe_2O_3^t$ contents of 13.3–59.1 wt.% correspond mainly to low-grade iron ores or ferruginous protore, whereas bulk MnO reaches 18.9 wt.% and magnetite contains an average of 3.1 wt.% MnO, indicating potential complex Fe–Mn mineralisation. Mineral assemblages record transitional amphibolite–granulite- to low-temperature granulite-facies conditions. The combined stratigraphic and geochemical evidence indicates episodic chemical precipitation in a volcanically influenced marine basin, interrupted by siliciclastic and volcaniclastic influx. Despite high-grade metamorphism conditions, primary seawater–hydrothermal signature was preserved. Staicele is therefore interpreted as an

Algoma-type BIF and represents the closest Latvian analogue of the Jõhvi and Bergslagen Fe–Mn systems, although a direct regional relationship requires geochronological confirmation.

Gārsene differs from Staicele in its higher iron grade and locally abundant Co-bearing pyrrhotite–pyrite mineralisation; magnetite-rich RMagQ contains an average of 76.5 wt.% $Fe_2O_3^t$. Mineral textures indicate an early high-grade metamorphic stage followed by amphibolite-facies retrogression, during which silica removal, magnetite recrystallisation, and sulphide remobilisation substantially upgraded and modified the ores. Geochemical variations reflect changing siliciclastic input, mineralogical controls, and secondary redistribution rather than persistent high-temperature hydrothermal activity. Gārsene is consequently interpreted as a strongly reworked, sediment-associated BIF with a tentative Superior-type affinity, whereas its primary depositional environment and regional relationship to Bergslagen remain less clearly preserved.

Acknowledgements

This research was financially supported by the Latvian Science Foundation project grant "Ore potential of metal-bearing crystalline basement rocks of central and eastern Latvia". Project No. lzp2023/1-0278.

Authors thank Shenghong Yang and Juha Köykkä for their constructive reviews and corrections, and Jussi S. Heinonen for valuable feedback on an earlier draft of the manuscript. We also thank Daiga Pipira (LVĢMC) for providing the samples.

Authorship contribution statement

D. Vorobjovs – supervision, writing, conceptualisation, investigation, methodology, data processing, data curation, interpretation, editing and illustration, sampling, sample preparation and analytical work; Ģ. Stinkulis – supervision, editing, and sample collection; M. Bērtiņš – analytical work (ICP–MS, XRF) and sample preparation; A. Vīksna – supervision of analytical work; R. Meija – analytical work (SEM–EDX); A. Brangule – analytical work (XRF).

Supplementary data

Supplementary data for this article is available via Zenodo data repository: https://doi.org/10.5281/zenodo.23001293 (Vorobjovs et al. 2026).

References

Alexander, B. W., Bau, M., Andersson, P. S. & Dulski, P., 2008. Continentally-derived solutes in shallow Archean seawater: Rare earth element and Nd isotope evidence in iron formation from the 2.9 Ga Pongola Supergroup, South Africa. Geochimica et Cosmochimica Acta 72, 378–394. https://doi.org/10.1016/j.gca.2007.10.028

Alibert, C., 2016. Rare earth elements in Hamersley BIF minerals. Geochimica et Cosmochimica Acta 184, 311–328. https://doi.org/10.1016/j.gca.2016.03.026

Allen, R. L., Lundström, I., Ripa, M. & Christofferson, H., 1996. Facies analysis of a 1.9 Ga continental margin, back-arc, felsic caldera province with diverse Zn-Pb-Ag-(Cu-Au) sulphide and Fe oxide deposits, Bergslagen region, Sweden. Economic Geology 91, 979–1008. https://doi.org/10.2113/gsecongeo.91.6.979

Basu, P., Ishwar-Kumar, C., Chaudhary, S., Chakrabarti, R., Satish-Kumar, M. & Sajeev, K., 2022. Major, trace element, and Nd isotopic compositions of banded iron formation and shales from the Sirsi shelf, Dharwar Craton, India: Implications for paleo-seawater chemistry, post-depositional alteration, and provenance. Precambrian Research 382, 106882. https://doi.org/10.1016/j.precamres.2022.106882

Bau, M. & Dulski, P., 1996. Distribution of yttrium and rare-earth elements in the Penge and Kuruman iron-formations, Transvaal Supergroup, South Africa. Precambrian Research 79, 37–55. https://doi.org/10.1016/0301-9268(95)00087-9

Bau, M. & Möller, P., 1993. Rare earth element systematics of the chemically precipitated component in Early Precambrian iron formations and the evolution of the terrestrial atmosphere-hydrosphere system. Geochimica et Cosmochimica Acta 57, 2239–2249. https://doi.org/10.1016/0016-7037(93)90566-F

Bekker, A., Slack, J. F., Planavsky, N., Krapez, B., Hofmann, A., Konhauser, K. O. & Rouxel, O. J., 2010. Iron formation: The sedimentary product of a complex interplay among mantle, tectonic, oceanic, and biospheric processes. Economic Geology 105, 467–508. https://doi.org/10.2113/gsecongeo.105.3.467

Beunk, F. F. & Kuipers, G., 2012. The Bergslagen ore province, Sweden: Review and update of an accreted orocline, 1.9–1.8 Ga BP. Precambrian Research 216–219, 95–119. https://doi.org/10.1016/j.precamres.2012.05.007

Bogdanova, S., Gorbatschev, R., Skridlaite, G., Soesoo, A., Taran, L. & Kurlovich, D., 2015. Trans-Baltic Paleoproterozoic correlations towards the reconstruction of supercontinent Columbia/Nuna. Precambrian Research 259, 5–33. https://doi.org/10.1016/j.precamres.2014.11.023

Bogatikov, O. A. & Birķis, A. P., 1973. Precambrian magmatism of western Latvia. Nauka, Moscow, 214 p. (in Russian)

Bolhar, R., Kamber, B. S., Moorbath, S., Fedo, C. M. & Whitehouse, M. J., 2004. Characterization of Early Archean chemical sediments by trace element signatures. Earth and Planetary Science Letters 222, 43–60. https://doi.org/10.1016/j.epsl.2004.02.016

Borromeo, L., Andò, S., Bersani, D., Garzanti, E., Gentile, P., Mantovani, L. & Tribaudino, M., 2023. How to identify pigeonite: A Raman and SEM–EDS study of detrital Ca-poor clinopyroxene from continental flood basalts. Chemical Geology 635, 121610. https://doi.org/10.1016/j.chemgeo.2023.121610

Brangulis, A. & Straume, J., 1984. Geology of the Latvian SSR. Zinātne, Rīga, 214 p. (in Russian)

Cao, C., Liu, X. M. & Chen, J., 2022. Cerium anomaly as a tracer for paleooceanic redox conditions: A thermodynamics-based Ce oxidation modeling approach. Frontiers in Earth Science 10, 927826. https://doi.org/10.3389/feart.2022.927826

Clout, J. M. F. & Simonson, B. M., 2005. Precambrian iron formations and iron formation-hosted iron ore deposits. In: Hedenquist, J. W., Thompson, J. F. H., Goldfarb, R. J. & Richards, J. P. (eds.), Economic Geology 100th Anniversary Volume, 1905–2005. Society of Economic Geologists, Littleton, Colorado, pp. 643–679. https://doi.org/10.5382/AV100.20

Conn, C. D., Spry, P. G., Layton-Matthews, D., Voinot, A. & Koenig, A., 2019. The effects of amphibolite-facies metamorphism on the trace-element composition of pyrite and pyrrhotite. Ore Geology Reviews 114, 103128. https://doi.org/10.1016/j.oregeorev.2019.103128

Craig, J. R. & Vokes, F. M., 1993. The metamorphism of pyrite and pyritic ores: An overview. Mineralogical Magazine 57, 3–18. https://doi.org/10.1180/minmag.1993.057.386.02

Damman, A. H., 1988. Exhalative-sedimentary manganiferous iron ores from the Gåsborn area, W. Bergslagen, Central Sweden. Geologie en Mijnbouw 67, 433–442.

Danielson, A., Möller, P. & Dulski, P., 1992. The europium anomalies in banded iron formations and the thermal history of the oceanic crust. Chemical Geology 97, 89–100. https://doi.org/10.1016/0009-2541(92)90137-T

Deer, W. A., Howie, R. A. & Zussman, J., 1992. An introduction to the rock-forming minerals. 2nd ed. Longman Scientific & Technical, London, 696 p.

Dreher, C. L., Schad, M., Robbins, L. J., Konhauser, K. O., Kappler, A. & Joshi, P., 2021. Microbial processes during deposition and diagenesis of banded iron formations. Paläontologische Zeitschrift 95, 593–610. https://doi.org/10.1007/s12542-021-00598-z

Ernst, D. M. & Bau, M., 2021. Banded iron formation from Antarctica: The 2.5 Ga old Mt. Ruker BIF and the antiquity of lanthanide tetrad effect and super-chondritic Y/Ho ratio in seawater. Gondwana Research 91, 97–111. https://doi.org/10.1016/j.gr.2020.11.011

Fettes, D. & Desmons, J., 2007. Metamorphic rocks: A classification and glossary of terms. Cambridge University Press, Cambridge, 244 p. https://doi.org/10.1017/CBO9780511628917

Frietsch, R., 1982. A model for the formation of the iron, manganese and sulphide ores of central Sweden. International Journal of Earth Sciences 71, 206–212. https://doi.org/10.1007/BF01825037

Ganeev, R. A., Kim, V. V., Vorobyov, D., Gross, U., Ubelis, A., Ozols, D., Butikova, J., Grube, J. & Sarakovskis, A., 2024. The first application of laser-induced breakdown spectroscopy: A fast-analytical technique in targeted search for elements in geological samples from deep boreholes in Latvia. Latvian Journal of Physics and Technical Sciences 61, 23–32. https://doi.org/10.2478/lpts-2024-0010

German, C. R. & Elderfield, H., 1990. Application of the Ce anomaly as a paleoredox indicator: The ground rules. Paleoceanography 5, 823–833. https://doi.org/10.1029/PA005i005p00823

Gourcerol, B., Thurston, P. C., Kontak, D. J., Côté-Mantha, O. & Biczok, J., 2016. Depositional setting of Algoma-type banded iron formation. Precambrian Research 281, 47–79. https://doi.org/10.1016/j.precamres.2016.04.019

Greber, N. D. & Dauphas, N., 2019. The chemistry of fine-grained terrigenous sediments reveals a chemically evolved Paleoarchean emerged crust. Geochimica et Cosmochimica Acta 255, 247–264. https://doi.org/10.1016/j.gca.2019.04.012

Gross, G. A., 1980. A classification of iron formations based on depositional environments. The Canadian Mineralogist 18, 215–222.

Hadji, F., Marok, A., Mokhtar Samet, A., Reolid, M. & Bensefa, K. E., 2024. Inorganic geochemistry of Miocene sediments from the Lower Chelif Basin (NW Algeria) for approaching weathering and paleoclimatic conditions. Journal of Iberian Geology 50, 137–156. https://doi.org/10.1007/s41513-024-00236-y

Holtstam, D. & Mansfeld, J., 2001. Origin of a carbonate-hosted Fe-Mn-(Ba-As-Pb-Sb-W) deposit of Långban-type in Central Sweden. Mineralium Deposita 36, 641–657. https://doi.org/10.1007/s001260100183

Indares, A. & Martignole, J., 1985. Biotite-garnet geothermometry in the granulite facies: The influence of Ti and Al in biotite. American Mineralogist 70, 272–278.

Johnson, C. M., Beard, B. L., Klein, C., Beukes, N. J. & Roden, E. E., 2008. Iron isotopes constrain biologic and abiologic processes in banded iron formation genesis. Geochimica et Cosmochimica Acta 72, 151–169. https://doi.org/10.1016/j.gca.2007.10.013

Justo, A. P., Dantas, E. L., Bau, M., Freitas-Silva, F. H., Santos, R. V. & Schorscher, J. H. D., 2020. Paleobasinal to band-scale REE + Y distribution in iron formations from Carajás, Amazon Craton, Brazil. Ore Geology Reviews 127, 103750. https://doi.org/10.1016/j.oregeorev.2020.103750

Karušs, J., Stinkulis, Ģ., Brants, M., Vorobjovs, D. & Zandersons, V., 2026. Economic potential for iron ores in the Precambrian basement of Latvia. Bulletin of the Geological Society of Finland. Advance online publication.

Kuršs, V. & Stinkule, A., 1997. Mineral resources in Latvia. University of Latvia, Rīga, 150 p. (in Latvian)

Li, F., Zhu, X., Ding, H. & Zhang, K., 2022. Local hydrothermal sources for Superior-type iron formations: Insights from the Animikie Basin. Precambrian Research 377, 106736. https://doi.org/10.1016/j.precamres.2022.106736

Mansfeld, J., 2001. Age and εNd constraints on the Paleoproterozoic tectonic evolution in the Baltic Sea region. Tectonophysics 339, 135–151. https://doi.org/10.1016/S0040-1951(01)00036-1

McLennan, S. M., 1989. Rare earth elements in sedimentary rocks: Influence of provenance and sedimentary processes. In: Lipin, B. R. & McKay, G. A. (eds.), Geochemistry and Mineralogy of Rare Earth Elements. Reviews in Mineralogy 21, Mineralogical Society of America, Washington, D.C., pp. 169–200.

Muhling, J. R., Gilbert, S. E. & Rasmussen, B., 2023. Rare earth element and yttrium (REY) geochemistry of 3.46–2.45 Ga greenalite-bearing banded iron formations: New insights into iron deposition and ancient ocean chemistry. Chemical Geology 641, 121789. https://doi.org/10.1016/j.chemgeo.2023.121789

Muwanguzi, A. J. B., Karasev, A. V., Byaruhanga, J. K. & Jönsson, P. G., 2012. Characterization of chemical composition and microstructure of natural iron ore from Muko deposits. ISRN Materials Science 2012, 174803. https://doi.org/10.5402/2012/174803

Ohta, A. & Kawabe, I., 2001. REE(III) adsorption onto Mn dioxide and Fe oxyhydroxide: Ce(III) oxidation by Mn dioxide. Geochimica et Cosmochimica Acta 65, 695–703. https://doi.org/10.1016/S0016-7037(00)00578-0

Philpotts, A. R. & Ague, J. J., 2009. Principles of igneous and metamorphic petrology. 2nd ed. Cambridge University Press, Cambridge, 684 p. https://doi.org/10.1017/CBO9780511813429

Planavsky, N., Bekker, A., Rouxel, O. J., Kamber, B., Hofmann, A., Knudsen, A. & Lyons, T. W., 2010. Rare earth element and yttrium compositions of Archean and Paleoproterozoic Fe formations revisited: New perspectives on the significance and mechanisms of deposition. Geochimica et Cosmochimica Acta 74, 6387–6405. https://doi.org/10.1016/j.gca.2010.07.021

Posth, N. R., Konhauser, K. O. & Kappler, A., 2011. Banded iron formations. In: Reitner, J. & Thiel, V. (eds.), Encyclopedia of Geobiology. Springer, Dordrecht, pp. 92–103. https://doi.org/10.1007/978-1-4020-9212-1_19

Prewitt, C. T. (ed.), 2018. Pyroxenes. Reviews in Mineralogy 7. De Gruyter, Berlin, 535 p.

Qian, G., Xia, F., Brugger, J., Skinner, W. M., Bei, J., Chen, G. & Pring, A., 2011. Replacement of pyrrhotite by pyrite and marcasite under hydrothermal conditions up to 220 °C: An experimental study of reaction textures and mechanisms. American Mineralogist 96, 1878–1893. https://doi.org/10.2138/am.2011.3691

Russo, S. C., McCoy-West, A. J. & Duuring, P., 2024. The potential for reconstructing primary ocean chemistry from hypogene and supergene altered banded iron formations: An example from Weld Range, Western Australia. Precambrian Research 413, 107573. https://doi.org/10.1016/j.precamres.2024.107573

Schopf, J. W., 1983. Earth's biosphere: Its origin and evolution. Princeton University Press, Princeton, New Jersey, 543 p.

Segliņš, V., Stinkule, A. & Stinkulis, Ģ., 2013. Mineral resources in Latvia. University of Latvia, Rīga, 184 p. (in Latvian)

Shi, K., Wang, C., Bagas, L. & Duan, H., 2024. Modified magnetite and hydrothermal apatite in banded iron-formations and implications for high-grade Fe mineralization during retrogressive metamorphism. American Mineralogist 109, 286–301. https://doi.org/10.2138/am-2022-8525

Soesoo, A., Nirgi, S., Urtson, K. & Voolma, M., 2021. Geochemistry, mineral chemistry and pressure-temperature conditions of the Jõhvi magnetite quartzites and magnetite-rich gneisses, NE Estonia. Estonian Journal of Earth Sciences 70, 71–93. https://doi.org/10.3176/earth.2021.05

Tamehe, L. S., Li, H., Ganno, S., Chen, Z., Lemdjou, Y. B. & Elatikpo, S. M., 2024. Insight into the origin of iron ore based on elemental contents of magnetite and whole-rock geochemistry: A case of the Bipindi banded iron formations, Nyong Complex, SW Cameroon. Journal of Earth Science 35, 16–28. https://doi.org/10.1007/s12583-022-1622-4

Tostevin, R., Shields, G. A., Tarbuck, G. M., He, T., Clarkson, M. O. & Wood, R. A., 2016. Effective use of cerium anomalies as a redox proxy in carbonate-dominated marine settings. Chemical Geology 438, 146–162. https://doi.org/10.1016/j.chemgeo.2016.06.027

Trendall, A. F., 2002. The significance of iron-formation in the Precambrian stratigraphic record. In: Altermann, W. & Corcoran, P. L. (eds.), Precambrian Sedimentary Environments: A Modern Approach to Ancient Depositional Systems. Blackwell Publishing, Oxford, pp. 33–66. https://doi.org/10.1002/9781444304312.ch3

Vetrennikov, V. V., 1984. Report on the study of iron ore formations in the Latvian SSR. 1st ed. Skrunda, 308 p. (in Russian)

Vetrennikov, V. V., 1991. Iron-siliceous formations of the Precambrian of Latvia and their forecasting evaluation. Zinātne, Rīga, 177 p. (in Russian)

Vorobjovs, D., Stinkulis, G., Bertins, M., Viksna, A., Meija, R., & Brangule, A., 2026. Electronic appendix A to "Mineralogical and geochemical characteristics and the genesis of the Paleoproterozoic Staicele and Gārsene Iron Ore Deposits of Latvia" [Data set]. Zenodo. https://doi.org/10.5281/zenodo.23001293

Walters, B. J., 2022. MinPlot: A mineral formula recalculation and plotting program for electron probe microanalysis. Mineralogia 53, 51–66. https://doi.org/10.2478/mipo-2022-0005

Wang, K., Shi, X., Zou, J., Liu, Y., Yao, Z. & Gorbarenko, S., 2021. Spatial distribution and provenance of detrital minerals of surface sediment in the Okhotsk Sea. Frontiers in Earth Science 9, 636850. https://doi.org/10.3389/feart.2021.636850

Yin, J., Li, H. & Xiao, K., 2023. Origin of banded iron formations: Links with paleoclimate, paleoenvironment, and major geological processes. Minerals 13, 547. https://doi.org/10.3390/min13040547

Yoshida, S., Ueda, H., Asanuma, H. & Sawaki, Y., 2024. Y–Ho fractionation during basalt alteration in hydrothermal system: An implication for superchondritic Y/Ho signature recorded in Precambrian banded iron formations. Chemical Geology 670, 122421. https://doi.org/10.1016/j.chemgeo.2024.122421

Zaronikola, N., Holley, E. A., Mathur, R. & Pace, D., 2023. Copper isotopes and constraints on the ore genesis process of Cu–Co ore deposits at the Idaho Cobalt Belt, USA. Minerals 13, 1355. https://doi.org/10.3390/min13111355

Zhang, Q., Sun, Y., Han, Y., Li, Y. & Gao, P., 2021. Producing magnetite concentrate via self-magnetization roasting in N_2 atmosphere: Phase and structure transformation, and extraction kinetics. Journal of Industrial and Engineering Chemistry 104, 571–581. https://doi.org/10.1016/j.jiec.2021.09.008